Nearshore subtidal bathymetry from time-exposure video images

S. G. J. Aarninkhof
Marine and Coastal Management, WL|Delft Hydraulics, Delft, Netherlands

B. G. Ruessink
Department of Physical Geography, Faculty of Geosciences, Institute for Marine and Atmospheric Research, Utrecht University, Utrecht, Netherlands

J. A. Roelvink[1]
Marine and Coastal Management, WL|Delft Hydraulics, Delft, Netherlands

Received 29 October 2004; revised 3 March 2005; accepted 23 March 2005; published 23 June 2005.

[1] Time-averaged (over many wave periods) nearshore video observations show the process of wave breaking as one or more white alongshore bands of high intensity. Across a known depth profile, similar bands of dissipation can be predicted with a model describing the time-averaged cross-shore evolution of organized wave and roller energy. This close correspondence between observed and modeled dissipation proxies is used to develop a new remote sensing technique, termed Subtidal Beach Mapper (SBM), to estimate nearshore bathymetry. SBM operates on a time series of cross-shore intensity profiles to resolve the pattern in depth change on a morphological timescale (including overall gain or loss of sediment) rather than to focus on the particular change induced by a single intensity profile. From each intensity profile, the breaking-induced component is isolated by removing the contribution of background illumination and persistent foam. The depth profile is updated based on a comparison between this video-derived dissipation proxy and a cross-shore profile of the dissipation of the roller energy. This updating is implemented through time-dependent mass balance equations for the seabed and a buffer layer above the bed. SBM was tested using 1 year of hourly video data collected at Egmond aan Zee, Netherlands. The dominant morphological changes observed from ground truth data were reproduced reasonably well, including the shoreward migration of the outer bar and the net sediment gain in the profile. Root-mean square differences between surveyed and SBM derived depth after 1 year of video-based depth updating with an average of about 70 intensity profiles per month were smallest ($\sim$0.2 m) on the inner bar and largest ($\sim$0.6 m) in the outer bar trough, with a profile average value of about 0.4 m. Despite the many processes included in SBM, the implementation of a heuristic scaling function in the mass balance equations to spatially adjust morphological growth rates was essential to these results, in particular near the shoreline, where otherwise the profile is prone to an unrealistic deepening.

Citation: Aarninkhof, S. G. J., B. G. Ruessink, and J. A. Roelvink (2005), Nearshore subtidal bathymetry from time-exposure video images, *J. Geophys. Res.*, *110*, C06011, doi:10.1029/2004JC002791.

1. Introduction

[2] The nearshore is a highly dynamic area where bathymetry may change on a wide range of spatial and temporal scales. Standard in situ bathymetric surveying techniques, such as ship-board sounding or amphibious vehicles, are usually too slow, expensive, and logistically difficult to apply in order to capture bathymetric change on all relevant timescales (days–years). In particular, these techniques do not allow the collection of data during periods of large waves and/or strong currents, when bathymetric changes are largest and of greatest scientific interest. Remote sensing techniques provide enhanced opportunities in this respect.

[3] Several remote sensing methods have been suggested to estimate nearshore bathymetry. One group of methods is based on light penetration in the water column and the subsequent reflection off the seabed, an overview of which is given by *Green et al.* [2000]. Multispectral [*Benny and Dawson*, 1983; *Bierwirth et al.*, 1993] and hyperspectral

[1] Also at Faculty of Civil Engineering and Geosciences, Delft University of Technology, Delft, Netherlands.

0148-0227/05/2004JC002791$09.00

[*Sandidge and Holyer*, 1998] technology, light detection and ranging (LIDAR) technology [*Irish and Lillycrop*, 1999], or combinations of these technologies [*Lyzenga*, 1985] have been applied to estimate depth from the received signals. The passive spectral techniques essentially rely on the principle that different (optical) wavelengths penetrate water to varying degrees. Using images collected by the Airborne Visible/Infrared Imaging Spectrometer (AVIRIS), *Sandidge and Holyer* [1998] retrieved depths over a depth range of 0 to 6 m in the Florida Keys area, with a root-mean square (rms) error of 0.39 m relative to ground truth data. With the active LIDAR system, water depth can be estimated from the time lapse between the sea surface and bottom return of the transmitted laser pulse. *Irish and Lillycrop* [1999] suggested a vertical accuracy of about 15 cm for their LIDAR-based SHOALS system, with a maximum measurable depth of up to 60 m. All these methods are often troubled by spatial variations in bottom type, which cause different substrate reflectance, and rely on optically clear water.

[4] A second group of methods estimates depth from depth-induced characteristics of the sea surface. This group can broadly be subdivided into methods that rely on (1) depth-induced spatial variations in surface roughness, (2) cross-shore changes in local wave number or wave celerity over a varying depth profile, or (3) cross-shore dissipation patterns caused by depth-induced wave breaking. In the first subgroup, interaction between strong (tidal) currents and bottom topography with crests perpendicular to this current causes modulations in the surface current velocity. These modulations, in turn, cause modulations in the wave spectrum, which can be monitored with radar [e.g., *Alpers and Hennings*, 1984; *Hennings*, 1990]. Examples of this technique have primarily been presented for sandbanks and sandwaves in the southern North Sea [e.g., *Hennings*, 1990; *Vogelzang et al.*, 1997], well seaward of the nearshore. An application to map nearshore bathymetry at the barrier island of Terschelling, Netherlands [*Calkoen et al.*, 1993] using ERS-1 Synthetic Aperture Radar (SAR) was not successful because the dominant morphological features (alongshore sandbars) were oriented in the direction of the currents and therefore did not result in clear spatial modulations of the radar backscatter.

[5] The second subgroup, often applied in nearshore studies, is based on the analysis of sequence of (instantaneous) images or cross-shore pixel arrays acquired with, for instance, shore-based [*Stockdon and Holman*, 2000] or airborne [*Williams*, 1947; *Dugan et al.*, 2001] optical systems, or X-band [*Bell*, 1999] or S-band [*McGregor et al.*, 1998] radar. Gradients in the phase difference between (processed) intensities at two closely spaced pixels provide an estimate of the local wave number, which then is inverted to depth using linear wave theory's dispersion relationship. Whereas depth estimates seaward of the breaker zone are accurate (*Stockdon and Holman* [2000] report typical errors of $\sim$5% of the observed water depth), wave nonlinearities and the difference in optical signatures of breaking and nonbreaking waves cause depth estimates farther onshore to be highly inaccurate. For instance, *Stockdon and Holman* [2000] show differences between estimated and observed depths of more than 1 m in depths <3 to 4 m. This is unfortunate, as it is within the breaker zone that spatial and temporal depth variations are largest, and accurate estimates are most urgently required. Examples of depth inversion using a dispersion relationship incorporating amplitude dispersion effects are given by *Grilli* [1998], *Kennedy et al.* [2000], and *Misra et al.* [2003]. However, *Grilli*'s [1998] approach is based on periodic, nonbreaking waves, not representative of natural surfzone conditions, and *Misra et al.*'s [2003] methodology, while capable of dealing with irregular waves, is restricted to nonbreaking conditions. Although *Kennedy et al.*'s [2000] technique is capable of handling irregular and breaking waves, its input data requirements can, at present, not be obtained realistically with remote sensing techniques.

[6] Finally, the third subgroup is, motivated by the pioneering work of *Lippmann and Holman* [1989] and, later on, *Van Enckevort and Ruessink* [2001], based on time-averaged (over many wave periods) optical [*Aarninkhof et al.*, 1997] or X-band radar [*Ruessink et al.*, 2002] images. The persistent wave-breaking on sandbars causes the time-averaged cross-shore intensity profile to show high-intensity peaks that closely resemble peaks of modeled [e.g., *Battjes and Stive*, 1985] breaking-wave dissipation. *Aarninkhof et al.* [1997] scaled observed intensity cross-shore profiles into profiles of the modeled dissipation proxy E_r/c^2, where E_r is the energy of the surface roller (the white aerated mass of water on a breaking-wave front) and c is phase speed, which were subsequently inverted to depth. Whereas results based on a rather limited model test for the single-barred beach at Duck, North Carolina, were quite promising (deviations of 10–20 cm near the bar crest and 30–40 cm in the bar trough), results for the double-barred beach at Noordwijk, Netherlands, were far less successful. Here the relative magnitude of the intensity maxima over the two bars was found to be opposite to the maxima of E_r/c^2, inducing erroneous depth estimates. Also, later work on the transformation of image intensity into an optical dissipation proxy [*Aarninkhof and Ruessink*, 2001] showed *Aarninkhof et al.*'s [1997] approach to be rather crude, incorporating the remnant foam [e.g., *Haller and Lyzenga*, 2003] contribution to the time-averaged image intensity.

[7] Our work is motivated by the desire to monitor nearshore bathymetric evolution over extended periods of time (>years) with a high temporal resolution (say, hours to days), providing a data base that will aid in the formulation and testing of nearshore system models. In this paper we present a new model concept aiming to extend existing capabilities [*Aarninkhof et al.*, 1997] of estimating cross-shore nearshore depth profiles from time-averaged shore-based video imagery, in particular focusing on multiple bar systems. The logistical ease and low cost of video imagery guarantees a long-term, high-resolution monitoring [*Holman et al.*, 1993], while the use of time-averaged intensity profiles provides most information in regions where bathymetric changes are expected to be largest and other methods [e.g., *Stockdon and Holman*, 2000] break down. In comparison to the model of *Aarninkhof et al.* [1997], both the technique to process image intensity into an observed dissipation proxy and the technique to transform this proxy into depth estimates were thoroughly revised.

Table 1. BIM Quality Criteria

Description	Egmond Value
I_0 is lower than $I_{0,\min}$, indicating poor lighting conditions or nighttime images.	$I_{0,\min} = 120$
$\Delta I = I - I_G$ exceeds $\Delta I_{\max}$, indicating a poor fit of I_G to I	$\Delta I_{\max} = 15.$
A_G of the highest peak does not exceed $A_{G,\min}$, indicating poorly pronounced dissipation peaks.	$A_{G,\min} = 20$
The σ_G of the widest peak exceeds $\sigma_{G,\max}$, indicating unrealistically wide dissipation peaks.	$\sigma_{G,\max} = 100$
The standard deviation of $I_b(x)$ is less than $\sigma_{b,\min}$, again indicating poorly pronounced dissipation peaks.	$\sigma_{b,\min} = 5$

After a description of the new model (section 2) it is tested against data collected at Egmond aan Zee, Netherlands, between September 1999 and September 2000 (section 3). The paper is finalized with a discussion of the Egmond results in section 4 and a summary of our main conclusions in section 5.

2. Model Formulations

2.1. General Concept

[8] The model, henceforth referred to as the Subtidal Beach Mapper (SBM), consists of two submodules. The first submodule, termed the Breaker Intensity Model (BIM), samples cross-shore intensity data from time-averaged video images, verifies their quality, and processes the data into a cross-shore profile of a normalized video-derived proxy of wave dissipation. This profile is the input into the second submodule, the Bathymetry Assessment Model (BAM). In this submodule, an initial depth profile, either surveyed or determined from a previous video image, is updated based on a comparison of the video-derived and modeled proxy of wave dissipation. Instead of quantifying depth profiles from a single image, as done by *Aarninkhof et al.* [1997], SBM adopts a time-dependent approach by operating on a time sequence of video images. With the time-dependent approach, BAM aims for a partial update of the bottom elevation on the basis of each single image, without achieving a perfect match between the video-derived and modeled dissipation proxy. Such a single image provides information on wave dissipation along a limited part of the profile only. The regions of information coverage vary with tidal variations in water level and changes in the offshore wave height [*Kingston et al.*, 2000; *Van Enckevort and Ruessink*, 2001]. Thus, by using multiple images with a temporal resolution less than the morphological timescale, the overall information coverage along the cross-shore profile improves, positively affecting SBM performance. The embedding of BAM in the framework of the overall time-dependent model SBM thus enables the resolution of the dominant temporal signal in the evolution of the video-observed patterns of wave breaking (i.e., on the morphological timescale) rather than focusing on the particular change resulting from a single image.

2.2. Pre-Processing of Image Intensity

[9] The image-intensity pre-processing module, or BIM, is described extensively by *Aarninkhof and Ruessink* [2004], and is therefore only briefly reiterated here. On a barred beach, a cross-shore intensity profile $I(x)$ sampled from a time-exposure image typically shows a background intensity level I_0, a linear trend with slope m_I, and a variable number of Gaussian-shaped features. The sum of I_0 and $m_I x$, where x is cross-shore distance, is related to background illumination, whereas the Gaussian-shaped features are associated with wave breaking over a sandbar or near the shore line. For the present work, only the Gaussian-shaped features are therefore of interest. To quantify and hence remove I_0 and $m_I\ x$ from $I(x)$, $I(x)$ is approximated as

$$I(x) \approx I_G(x) = I_0 + m_I x + \sum_{i=1}^{N_G} G_i(x), \tag{1}$$

in which N_G is the number of Gaussian peaks $G(x)$, which, in turn, are given by

$$G(x) = A_G \exp^{-\left(\frac{x-\mu_G}{\sigma_G}\right)^2}, \tag{2}$$

where A_G, μ_G, and σ_G represent a measure for the height, mean location, and width, respectively, of a Gaussian peak. Values of I_0, m_I, and of A_G, μ_G, and σ_G for each peak were computed using nonlinear least squares data fitting by the Gauss-Newton method.

[10] The description of I_x by $I_G(x)$ also allows imposition of a number of objective criteria to interpret the quality of $I(x)$. For example, a $I_G(x)$ with the estimated A_G of the highest Gaussian peak below a user-defined threshold indicated the absence of wave breaking. Table 1 lists the criteria used to assess the quality of the observations.

[11] From a good-quality $I_G(x)$ the breaking-induced intensity $I_b(x)$ was taken as the series of Gaussian peaks, thereby removing the background illumination described by $I_o + m_I x$. Two sources of white foam contribute to $I_b(x)$ [e.g., *Haller and Lyzenga*, 2003; *Aarninkhof and Ruessink*, 2004]. The first is the foam associated with the aerated roller at the face of a breaking wave, and the second is the foam that escapes from the water column after being trapped in the column during the breaking process and that subsequently remains floating on the sea surface for up to several wave periods. Clearly, only the roller-induced contribution to $I_b(x)$ is relevant to the present work and therefore needs to be isolated by removing the intensity contribution of relict foam. Here the foam-removal technique introduced by *Aarninkhof and Ruessink* [2001] and extended by *Aarninkhof and Ruessink* [2004] is applied. In this technique, $I_b(x)$ is transformed into the roller-induced intensity $I_r(x)$ by multiplying $I_b(x)$ by a cross-shore varying factor that scales with the coefficient of variation V of I_b at the location where I_b attains its maximum value. (The standard deviation required to compute V is available from routinely collected variance images.) As shown in detail by *Aarninkhof and Ruessink* [2004], a low (high) V is indicative of a large (small) amount of relict foam. The scale

factor also incorporates the free parameter p, which, when decreased, increases the scaling factor, and which can realistically vary in the range from 1 to 20; see *Aarninkhof and Ruessink* [2004] for further details. Finally, $I_r(x)$ is normalized as

$$I_{r,n}(x) = \frac{I_r(x)}{\int_x I_r(x)\mathrm{d}x}, \tag{3}$$

which is used as input into the second submodule of SBM, BAM.

2.3. Bathymetry Estimation

[12] Within the context of the overall time-dependent model SBM, the submodule BAM governs the morphodynamic updating of a cross-shore profile based on vertical sediment fluxes, driven by differences between a video-derived dissipation proxy $D_o(x)$ and a model-predicted dissipation proxy $D_c(x)$, both of which are defined below. BAM adopts a two-layer approach, consisting of the seabed with elevation $z(x)$ and a sediment buffer layer with sediment availability $C_s(x)$, representing a sediment volume per unit area. The cross-shore coordinate x is defined positive in the onshore direction, and the elevation z is positive upward, with $z = 0$ where the profile intersects mean sea level; the (positive) water depth d is $d = \zeta - z$, where ζ is the tidal water level. A positive difference $D_c - D_o$ drives an upward directed erosional sediment flux S_E from the seabed to the buffer layer, causing local erosion of the seabed and a local increase in C_s. A negative $D_c - D_o$ results in the opposite effect, driving a downward direct accretional sediment flux S_A which yields accretion of the seabed and a C_s decrease in the buffer layer. Cross-shore gradients in $C_s(x)$ drive the horizontal redistribution of sediment within the buffer layer from areas of high C_s (sediment surplus in the buffer layer due to seabed erosion) to regions of low C_s (sediment shortage in the buffer layer due to seabed accretion). The sediment buffer layer was included to guarantee conservation of mass within the overall system. Notice that C_s is not related to any physical process and only provides a sediment buffer to enable erosion and accretion of the seabed, while facilitating the redistribution of sediments within the nearshore.

[13] BAM operates on a real-world time frame t, using a variable number of time steps with pre-defined spacing Δt to bridge the time gap $t_1 - t_0$ between successive, good-quality video images collected at t_0 and t_1. Every time t, the bathymetry $z(x, t)$ is estimated by updating the previous bathymetry $z(x, t - \Delta t)$ on the basis of a time-dependent vertical sediment flux $S(x, t)$ driven by differences between $D_c(x, z(t - \Delta t), t_1)$ and $D_o(x, t_1)$. D_c is computed from the tide and wave conditions at time t_1 using the bathymetry at time $t - \Delta t$. To describe these processes mathematically, BAM solves time-dependent mass balance equations for the seabed

$$\frac{\partial z(x,t)}{\partial t} = -[S_E(x,t) + S_A(x,t)] \tag{4}$$

and the buffer layer

$$\frac{\partial C_s(x,t)}{\partial t} - D\left(\frac{\partial^2 C_s(x,t)}{\partial x^2}\right) = S_E(x,t) + S_A(x,t), \tag{5}$$

respectively. In equations (4) and (5), $S_E(x, t)$ and $S_A(x, t)$ represent the erosional and accretional sediment fluxes per unit area and per unit time including pores. The model formulations for S_E and S_A, which are applicable to regions where $D_c > D_o$ and $D_c < D_o$, respectively, are

$$S_E(x,t) = w_E F_s(x)[D_c(x, z(t-\Delta t), t_1) - D_o(x, t_1)] \tag{6}$$

$$S_A(x,t) = w_A F_s(x)\left[\frac{C_s(x,t)}{C_{\mathrm{s,max}}(t)}\right] D_c(x, z(t-\Delta t), t_1) - D_o(x, t_1)], \tag{7}$$

respectively, where w_E is the erosion parameter governing the timescale of bottom erosion, w_A is the accretion parameter affecting the timescale of accretion, $C_{\mathrm{s,max}}(t)$ is the cross-shore maximum of $C_s(x, t)$ at time t, and $F_s(x)$ is a scaling function defined below. As can be seen from equations (6) and (7), both S_E and S_A are driven by differences between D_c and D_o. In addition, S_A also depends on the local sediment availability $C_s(x, t)$ normalized by $C_{\mathrm{s,max}}(t)$. S_A approaches zero for very low C_s, thus preventing the occurrence of negative C_s in the buffer layer. Arbitrary settings of w_E and w_A generally yield an overall erosion $\int S_E \mathrm{d}x$ which differs from the overall accretion $\int S_A \mathrm{d}x$, thereby allowing for the modeling of erosional or accretional nearshore systems. As the overall system of seabed and sediment buffer layer is mass conservative (the source terms in equations (4) and (5) are equal and opposite), erosion (accretion) of the seabed is associated with a gain (loss) of sediment in the buffer layer. To model nearshore systems with no net erosion or accretion at the seabed, the parameters w_E and w_A can be set such that $\int S_E \mathrm{d}x$ equals the overall accretion $\int S_A \mathrm{d}x$ at every Δt. The diffusion term in equation (5) with diffusion coefficient D accounts for the redistribution of sediments in the buffer layer. The boundary conditions used at the seaward and shoreward end of the model are $\partial z/\partial x = 0$ and $\partial^2 C_s/\partial x^2 = 0$, implying that BAM does not allow for changes in bathymetry at the seaward and shoreward end of the model, nor for diffusive sediment fluxes across the boundaries of the buffer layer.

[14] Following *Aarninkhof and Ruessink* [2004], D_c is set equal to the dissipation of roller energy D_r computed using the wave model outlined in Appendix A. The parameter D_o is obtained by scaling $I_{r,n}$ with the incoming wave energy flux to arrive at a quantitative match of D_c and D_o. Thus

$$D_c(x, z(t-\Delta t), t_1) = D_r(x, z(t-\Delta t), t_1) \tag{8}$$

$$D_o(x, t_1) = E_0 c_{\mathrm{gx}} I_{r,n}(x, t_1), \tag{9}$$

where $E_0 = 0.125\rho g H_{\mathrm{rms}}^2$ is the wave energy at deep water and c_{gx} is the cross-shore component of the wave group velocity, also at deep water.

[15] The scaling function $F_s(x)$ is heuristically given by

$$F_s(x) = 0.5\left[\tanh\left(\frac{120h(x)}{L_{\mathrm{deep}}} - \frac{15h_{\mathrm{deep}}}{L_{\mathrm{deep}}}\right) + 1\right]\left[\frac{h(x)}{h_0}\right]^q, \tag{10}$$

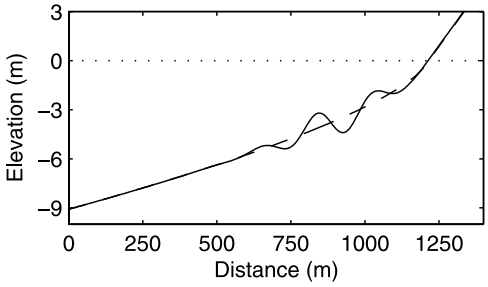

Figure 1. Initial nonbarred (dashed line) and target (solid line) elevation profile z versus cross-shore distance x used to illustrate SBM behavior.

where $h(x)$ is local water depth, h_0 is the water depth at the seaward boundary of the model, L_{deep} is a representative deep water wavelength for the field site under consideration, h_{deep} is a representative water depth near the outer end of the surf zone, and q is a coefficient. L_{deep} and h_{deep} are considered as field site representative parameters that do not vary with changing environmental conditions. The ratio of $h(x)$ to h_0 forces F_s to stimulate morphological changes in the deeper trough regions as compared to the relatively shallow bar regions. The tanh-part reduces F_s to zero near the shoreline where the phase velocity c approaches zero, which causes D_r to become large owing to its proportionality to E_r/c and BAM to show unrealistic behavior. The relevance of $F_s(x)$ to SBM performance is discussed further in section 4.1.

[16] In practice, the gap $t_1 - t_0$ will be highly variable because of the presence of nighttime images, periods of no waves, and missing wave data. Bridging gaps of, say, more than 1–2 days is equivalent to forcing SBM to overfit on the single image available at t_1. Because this is inconsistent with our viewpoint that SBM should not focus too much on the particular characteristics of a single image, we decided to allow SBM to update bathymetry only for a maximum period T_u, which is expected to be of the order of 12 to 36 hours. When $t_1 - t_0 \leq T_u$, sbm updates the bathymetry all the way up to $t = t_1$. If, in contrast, $t_1 - t_0 > T_u$, then bathymetry updating is performed for the first T_u hours only, implying that the estimated elevation profile at t_1 is set equal to the one estimated at $t = T_u$.

2.4. Synthetic Example

[17] We illustrate model behavior by applying SBM to reconstruct a known, time-independent bar-trough depth profile $z(x)$ from an initially ($t = 0$) nonbarred profile (Figure 1). The $D_o(x)$ time series were time series of $D_r(x)$ computed (Appendix A) with the target-bar trough profile using shore-normal waves with a time-independent offshore root-mean square wave height of 1 m and peak period of 6.5 s, and 12-hour varying offshore water level with a 1-m amplitude. $D_o(x)$ series were provided to SBM with a time step of 1 hour.

[18] Model behavior is illustrated in Figure 2 using Δt = 360 s, $w_E = 2.5 \times 10^{-5}$ ms^2/kg, $D = 0.1$ m^2/s, an initial sediment availability of $C_s = 1$ m^3/m^2 along the entire profile, $L_{\text{deep}} = 60$ m, $h_{\text{deep}} = 8$ m, $T_u = 1$ hour, and the restriction of mass-conservation at the seabed, which demands that the overall erosion $\int S_E dx$ equals the overall accretion $\int S_A dx$ at every Δt. Deviations $D_c - D_o$ (equations 8 and 9) drive a sediment flux $S_0 = S_E + S_A$, which causes accretion of the seabed in the bar regions and erosion in the trough regions, with an associated decrease and increase in C_s, respectively, in the buffer layer. No bathymetric changes occur outside the regions of wave dissipation. Diffusion induces a redistribution of sediment in the buffer layer, as can be seen from the flattening of the cross-shore distribution of C_s. Deviations $D_c - D_o$ and $\Delta z = \hat{z}(x, t) - z(x)$, where the $\hat{}$ symbol indicates a modeled profile, decrease rapidly during the first few hours to near-zero values at the end of the simulation. At that time, $C_s(x)$ is approximately cross-shore constant at 1 m, identical to the initial C_s distribution at $t = 0$ and confirming the conservation of mass at the seabed and in the buffer layer. Owing to the application of F_s, the model response time is rather small in the outer bar region, increasing in shallower water. Furthermore, it can be observed that the timescale of profile adjustment in the trough regions is large relative to the neighboring bar regions. This is caused by the fact that sediment accretion in the bar regions is associated with large deviations $D_c - D_o$ along relatively small parts of the beach profile. The compensating erosion of sediment is driven by smaller deviations $D_c - D_o$ along larger portions of the beach profile.

[19] Sensitivity tests, reported in detail by *Aarninkhof* [2003], show that the timescale of profile adjustment is governed by w_E, w_A, and q. In mass-conservative mode the morphological changes per unit time increase with an increase in w_E (and, hence, w_A) and a decrease in q. When SBM was applied in nonconservative mode (with $w_E = 2.5 \times 10^{-5}$ ms^2/kg), *Aarninkhof* [2003] noted that SBM behavior is rather sensitive to w_A. Small w_A ($<1 \times 10^{-5}$ ms^2/kg) hamper the generation of sandbars, while large w_A ($>5 \times 10^{-5}$ ms^2/kg) hamper the deepening of the trough regions. The resulting profile deviations particularly occur in shallow water depths and negatively affect model performance (see also section 4.1). In tests in which w_E and w_A were varied simultaneously, SBM managed to reconstruct the target bar-trough elevation profile from the initially nonbarred profile when w_E and w_A differed by less than a factor of 2, albeit that the time required increased with increasing relative differences between w_E and w_A. For an initial sediment availability $C_s = 1$ m^3/m^2, SBM performance was found to be virtually unaffected by D [*Aarninkhof*, 2003]. For $C_s = 0.25$ m^3/m^2, the sensitivity to D increased because a decrease in D hampers bar generation owing to a limited sediment availability for accretion. Even for such a small initial C_s, however, model sensitivity to D is small compared to the sensitivity to w_E, w_A, or q [*Aarninkhof*, 2003].

3. Field Test

3.1. Data Set Description

[20] In this section the technique to infer the temporal bathymetry from time-exposure video images is tested against data collected at Egmond aan Zee, Netherlands, between September 1999 and September 2000. The Egmond site is located at the approximately north-south oriented central Dutch coast, facing the semi-enclosed North Sea. The yearly averaged significant offshore wave

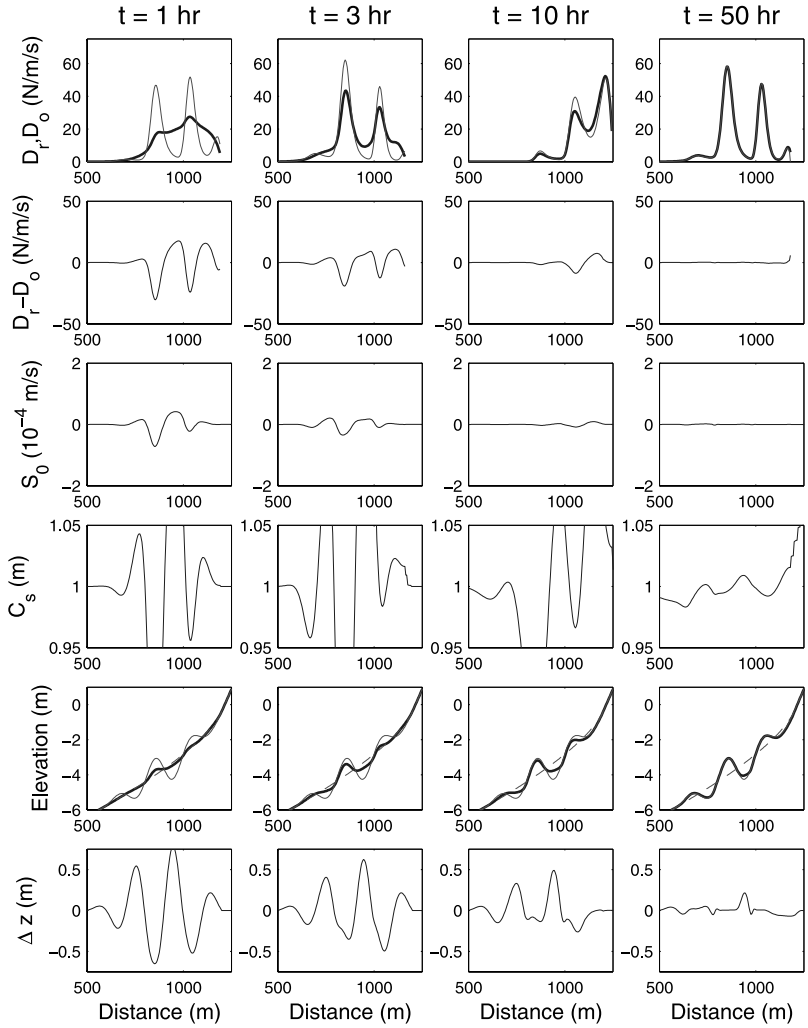

Figure 2. BAM results for the reference case versus cross-shore distance after (first column) 1, (second column) 3, (third column) 10, and (fourth column) 50 hours: (first row) D_c and D_o, (second row) deviations $D_c - D_o$, (third row) sediment flux $S_0 = S_E + S_A$, (fourth row) C_s, (fifth row) bed elevation z, and the profile deviations $\Delta z = \hat{z} - z$. Thick lines in the first and fifth row are BAM predictions, thin lines represent D_o (first row) and the target z (fifth row). The dashed line in the fifth row is the initial nonbarred profile.

height is about 1.2 m, with a mean period of 5 s. Waves predominantly approach the shore from south-westerly and north-westerly directions. The range of the semi-diurnal tide is, on average, 1.65 m, varying from 1.4 m at neap tide to about 2.0 m at spring tide. Two subtidal sandbars dominate the nearshore bathymetry. In August 1999 a shoreface nourishment of 400 m^3/m was implemented on the seaward side of the outer bar over an alongshore length of 2200 m.

[21] To monitor the effect of the nourishment on the bathymetry, a 5-camera Argus station was installed on top of the Jan van Speyk lighthouse and the amphibious WESP [*Ruessink et al.*, 2000] performed three bathymetric surveys (30 September 1999, 17 May 2000, and 28 August 2000), typically along 50 cross-shore profiles with a 100-m spacing. Here, time-exposure images sampled hourly by the offshore-directed camera 3 and the northward-oriented camera 1 were used to quantify changes in depth along a central array $y = -130$ m and a northern array $y = -1500$ m, respectively (Figure 3), where y is local alongshore Argus coordinate. The cross-shore line at $y = -130$ m extended 900 m offshore from with a 5-m spacing, where the line at $y = -1500$ m extended some 700 m offshore with the same spacing. Using the known geometry of the image, the list of sampling locations (x_i, y_i, z_i), where z_i is the water level measured at an offshore tide station, was converted to the pixel coordinate (u_i, v_i) from which image intensity I was sampled (Figure 3). The cross-shore profile of I was then resampled to the cross-shore model grid. About 700 (1000) $I(x)$ at $y = -130(-1500)$ m were considered suitable for further processing by SBM based on the criteria in Table 1. This corresponds to 60 to 80 good-quality $I(x)$ per month.

[22] Wave data (offshore H_{rms}, T_p, and $\bar{\theta}$) for the 1-year test period were collected hourly by a directional wave buoy, located approximately 15 km south of Egmond. Missing wave data were replaced by values from a wave buoy approximately 75 km to the north. Unfortunately, no wave data were available for the period 18 October to 17 November 1999, causing SBM to be nonapplicable during this period.

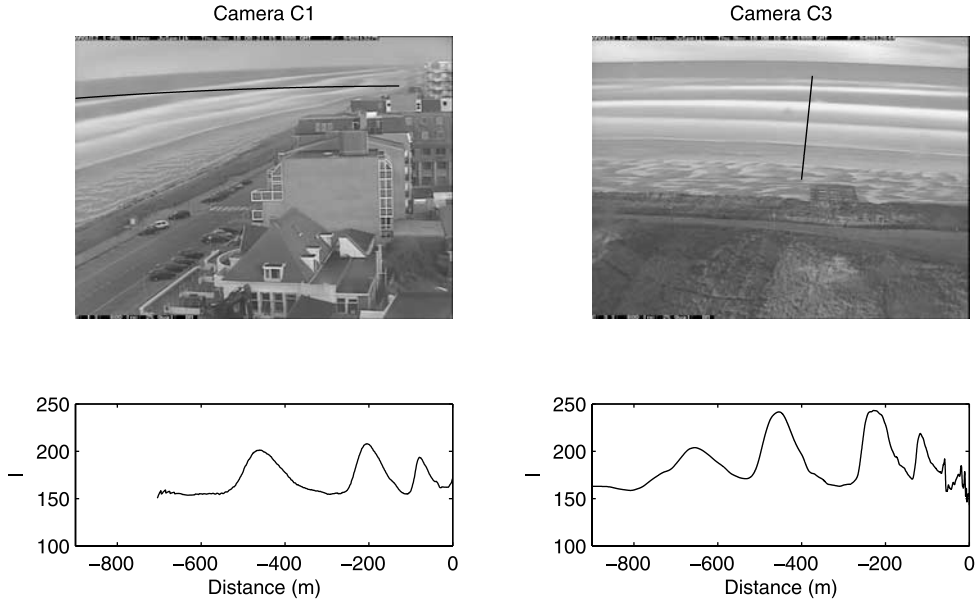

Figure 3. (top) Cross-shore sampling lines in cameras C1 ($y = -1500$ m) and C3 ($y = -130$ m). (bottom) Intensity profiles sampled from these two specific images, collected on 18 November 1999, 0800 UT. In each case, $x = 0$ is located on the beach.

Estimates of offshore water level were obtained by averaging observations at two tidal stations separated in the alongshore by 30 km and centered around Egmond.

3.2. Results

[23] Using the depth profiles surveyed in September 1999 as the initial profiles, reasonable agreement between modeled and measured bathymetry on 14 May and 28 August 2000 was found for $p = 1$, $w_E = 1 \times 10^{-7}$ ms^2/kg, $w_A = 2.5 \times 10^{-7}$ ms^2/kg, $q = 1.5$, and $T_u = 24$ hours. With these free model parameter values, SBM is capable of reproducing the shoreward migration of the outer bar and the net accumulation of sand in the inner nearshore in the $y = -130$ m profile (Figure 4). Note that both w_E and w_A differ by 2 orders of magnitude from the values in the synthetic example. The Egmond field test started with a measured barred profile and, as opposed to the synthetic example, did not require high w_E and w_A to (quickly) generate bars from a barless profile.

[24] After 1 year of video-based bathymetry updating, the deviations between measured and modeled depth at the (subtidal) bar crest are 5–15 cm, increasing to 20–40 cm at the seaward face of the bars (Figure 4). Although the model shows a tendency toward accretion in shallow water, the present parameter settings do not enable the model to reproduce the generation of the intertidal bar over the summer period (x near -75 m, Figure 4). Further stimulating morphological changes in shallow water through a decrease in q yielded improved model performance for $y = -130$ m, but invoked unrealistically large accretion in the

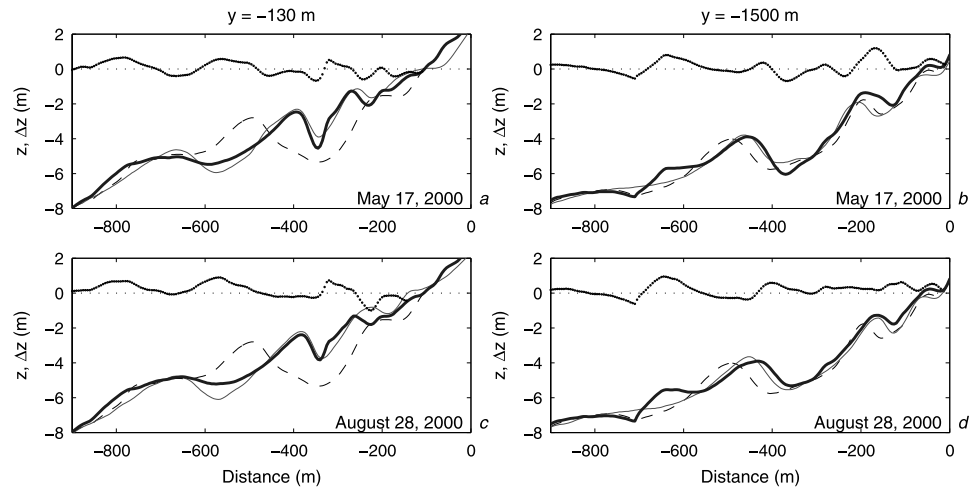

Figure 4. Modeled (thick line) and surveyed (thin line) elevation z, and their difference Δz (dotted line) versus (left) cross-shore distance at $y = -130$ m and (right) $y = -1500$ m on (a, b) 17 May 2000 and (c, d) 28 August 2000. The dashed line in each plot is the initial profile surveyed in September 1999.

Table 2. Accuracy of Depth Estimate

Profile Line	$\overline{\Delta z}$, m	Δz_{rms}, m	$\overline{R}$	R_{rms}
		May 2000		
$y = -130$ m	0.01	0.35	−0.068	0.211
$y = -1500$ m	0.11	0.40	0.084	0.253
		August 2000		
$y = -130$ m	0.14	0.43	−0.041	0.261
$y = -1500$ m	0.17	0.37	0.094	0.228
		All data		
$y = -130$ m	0.08	0.39	−0.055	0.237
$y = -1500$ m	0.14	0.39	0.089	0.241

inner nearshore of the $y = -1500$ m transect. In the trough regions, the water depth is generally underestimated, except for the inner trough in May 2000. On the seaward face of the nourishment (around $x = -800$ m in $y = -130$ m and $x = -700$ m in $y = -1500$ m) the model predicted an erroneous accretion of about 1 m, while the surveyed profiles indicate a 100 m onshore migration of the nourishment to become the new outer bar (Figure 4). In terms of volume changes between the −5 and 0 m depth contours at $y = -130$ m, the model finds a net accretion of 194 (236) m^3/m after 8 (12) months, comparing favorably with the measured accretion of 244 (195) m^3/m with respect to the initial profile. In more detail, the model underpredicts the net accretion found in the field during the first 8 months, particularly at shallow water depths ($x \approx -100$ m, Figure 4a). In the final 4 months, the model predicts ongoing accretion (50 m^3/m), whereas the field data show a net erosion of sediment between the −5 and 0 m depth contours (41 m^3/m). The latter mismatch is attributed to the underprediction of the water depth in the outer trough region ($x \approx -600$ m, Figure 4c), which is associated with a net accretion of 16 (78) m^3/m after 8 (12) months. Deviations rapidly increase in the final 4 months, owing to the lack of wave dissipation information during the calm summer period. Apart from this mismatch, the model correctly represents tendencies of accretion and erosion along the subtidal part of the profile.

[25] Model performance was measured by the difference between the modeled and measured elevations ($\hat{z}(x, t)$ and $z(x, t)$, respectively),

$$\Delta z(x,t) = \hat{z}(x,t) - z(x,t), \tag{11}$$

and the relative errors,

$$R(x,t) = \frac{\hat{z}(x,t) - z(x,t)}{d(x,t)}. \tag{12}$$

Because z is defined to be negative below MSL, positive Δz indicates an underestimation of the local water depth. In equation (12), $\Delta z(x, t)$ is normalized with the local (positive) water depth. The profile-averaged offsets $\overline{\Delta z}$ and $\overline{R}$ are

$$\overline{\Delta z}(t) = \frac{1}{N_x}\sum_{i=1}^{N_x} \Delta z(x,t) \tag{13}$$

$$\overline{R}(t) = \frac{1}{N_x}\sum_{i=1}^{N_x} R(x,t). \tag{14}$$

Only Δz and R for $z(x, t) < 0$ are taken into account. The rms error of the differences, calculated as

$$\Delta z_{rms}(t) = \sqrt{\frac{1}{N_x}\sum_{i=1}^{N_x} (\Delta z(x,t))^2} \tag{15}$$

$$R_{rms}(t) = \sqrt{\frac{1}{N_x}\sum_{i=1}^{N_x} (R(x,t))^2}, \tag{16}$$

is used to measure the variability of the differences.

[26] As can be seen in Table 2, error statistics, except for $\overline{R}$, were almost identical for both profile lines. This is encouraging because the intensity profiles involved were sampled from two different cameras. It is obvious from Table 2 that the model overestimates the overall accretion in both profiles, indicated by the positive $\overline{\Delta z}$. Δz_{rms} is about 0.4 m, and the relative RMS errors R_{rms} are typically 0.2–0.25 (Table 2), implying that the RMS profile deviations typically amount to 20 to 25% of the local water depth.

[27] To examine SBM performance along different parts of the profile, the $y = -130$ m profiles were divided into six parts, as demonstrated for the August 2000 profile in Figure 5, representing the outer bar, the outer trough, the

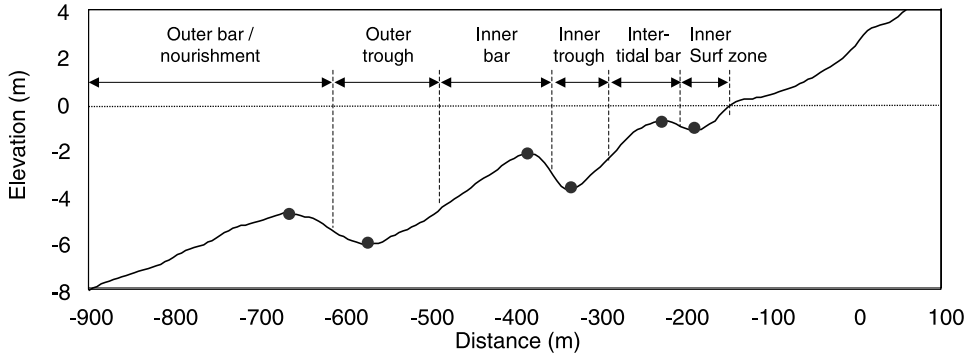

Figure 5. Subdivision of an elevation profile in six regions for separate evaluation of SBM performance. The boundaries of each region are chosen at the midpoint between the neighboring bar crest and bar trough, both indicated with dots.

Table 3. Model Error Statistics for Different Parts of the Profile ($y = -130$ m, Both Observations)

Profile Part	$\overline{\Delta z}$, m	Δz_{rms}, m	$\overline{R}$	R_{rms}
Outer bar	0.20	0.37	0.028	0.058
Outer trough	0.47	0.52	0.080	0.087
Inner bar	−0.19	0.22	−0.063	0.070
Inner trough	0.07	0.46	0.029	0.131
Intertidal bar	−0.26	0.50	−0.253	0.446
Inner surf zone	−0.25	0.29	−0.384	0.514

inner bar, the inner trough, the intertidal bar, and the inner surf zone up to $z = 0$ m. With a Δz_{rms} of 0.22 m (considering both observations, Table 3), the model performs well in the inner bar region. The statistics confirm the rather poor performance at the intertidal bar, with a Δz_{rms} of above 0.5 m and an R_{rms} of about 0.45 (all data). A similar Δz_{rms} was found for the outer trough. On the whole, SBM appears to underestimates water depths in the trough regions (positive $\overline{\Delta z}$) and overestimates water depths in the bar regions (negative $\overline{\Delta z}$). As expected, relative errors increase with decreasing water depth (Table 3).

3.3. Sensitivity Tests

[28] To assess the dependence of the results to the magnitude of the model's free parameters, various sensitivity tests (using $y = -130$ m only) were carried out in which one of the model parameters was varied while the others were kept constant at their values used in the previous subsection. The results of these test are described below in a qualitative sense.

[29] A change in w_E and w_A, while keeping the ratio w_A/w_E constant, affects the timescale of profile adjustment changes but not the overall patterns of erosion and sedimentation. This implies that tendencies toward erosion or accretion become more apparent with an increase in w_E and w_A. For $y = -130$ m this means that such an increase is associated with an increase in the erroneous accretion at the seaward side of the shoreface nourishment, additional erosion at the seaward face of the inner bar, and additional accretion in the inner trough region, across the intertidal bar and in the inner surf zone. A change in the ratio w_A/w_E, however, directly affects the patterns of erosion and sedimentation along the beach profile. The results obtained from varying the ratio w_A/w_E over the range 1.5–2.5 confirm that the tendencies toward accretion at the seaward side of the shoreface nourishment, in the trough regions, and in shallow water are stimulated with an increase in w_A/w_E.

[30] Lowering q implies a depth-dependent increase in the timescale of profile adjustment, the effect of which increases with decreasing water depth. Variation of q over the range 1.0–2.5 shows that small q particularly stimulate the tendency toward accretion in the region of the intertidal bar. However, existing tendencies toward erosion or accretion at deeper parts of the surf zone are also stimulated, albeit less rigorously. This is observed from a slight increase in the erroneous accretion seaward of the shoreface nourishment and some additional erosion of the seaward face of the inner bar for small q.

[31] To assess SBM sensitivity to p, p was varied over the range 0.5–5.0. The model outcome shows a deepening of the trough regions and the seaward face of the breaker bars with decreasing p. This is induced by a narrowing of the peaks of D_o, resulting from a more rigorous correction for the effect of persistent foam. Small p (= 0.5) yields an appreciable increase in the accretion in a narrow region around the bar crest. However, owing to the narrowing of the D_o peaks, D_c increasingly overestimates the corresponding D_o at both sides of the dissipation maximum, which yields a deepening of the trough regions and the bar face. The opposite situation occurs for large p, which induces a nonrealistic flattening of the overall beach profile. A decrease in p was further found to stimulate bar generation in shallow water, while it hampers bar formation at deeper water.

[32] SBM sensitivity to variations of T_u is primarily observed along regions which are less frequently exposed to wave breaking. Taking $T_u = 36$ hours shows, for instance, a slight increase in the accretion in deep surf zone section and at very shallow water, relative to a run with $T_u = 12$ hours. This implies that large T_u improves SBM performance for $y = 130$ m in the shallow surf zone, while the deep section benefits from lower T_u. On the whole, SBM sensitivity to T_u over the range tested here is less than to the other four parameters.

4. Discussion

4.1. Performance

[33] The SBM application to the Egmond field case has demonstrated the model's capability to reproduce the dominant morphological changes during the first year after placing a shoreface nourishment, including the shoreward migration of the outer bar and the net accretion of sand in the nearshore part of the surf zone. Obtained Δz_{rms} typically amounted to 0.4 m (Table 2) and relative errors R_{rms} increase with decreasing water depth. Furthermore, SBM shows a tendency to overestimate the overall accretion across the surf zone for the present data set.

[34] Detailed investigation of the calculated profile evolution over 1 year (Figure 6) demonstrates that profile deviations at deeper water ($x = -800$ m) are induced by the inclusion of a limited number of poor-quality dissipation profiles D_o. For reasons unexplored yet, some early morning time exposure images showed a bright, wave dissipation-like band of high intensity at deep water under very mild wave conditions, meeting our acceptance criteria, but clearly not representing true dissipation bands. Further investigation on the intensity characteristics of error-inducing images is necessary to arrive at a robust criterion for their rejection. Once the bathymetry had been adjusted to these inaccurate $D_o(x)$, no images provided the erosional difference $D_c - D_o$ to remove the erroneous accretion at deeper water again. The latter observation also applies to the outer trough region ($x = -550$ m), where SBM gradually lowers the bed elevation over the period September 1999 to April 2000 (Figure 6). From April 2000, there appear to be no images anymore that yield a $D_c - D_o$ to induce the desired further lowering of the outer trough. Instead, some $D_o(x)$ cause a minor accretion of the outer trough region during the summer period. Similar tendencies are observed in the inner trough region ($x = -325$ m), where the accumulation of small errors also yields an erroneous accretion over the summer period. Further note that the

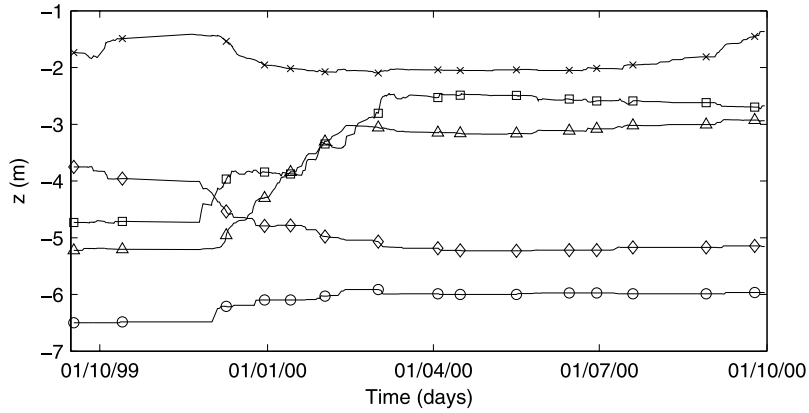

Figure 6. Elevation z in $y = -130$ m versus time at $x = -800$ m (circles), $x = -550$ m (diamonds), $x = -400$ m (squares), $x = -325$ m (triangles), and $x = -225$ m (crosses); see also Figures 4 and 5. Note that the markers are plotted every fiftieth data point.

inner surf zone time series at $x = -225$ m shows a favorable increase in the bed elevation in September 2000, which compensates for the vertical offset in the inner surf zone at August 28 that was reported earlier (Figure 4).

[35] Thus profile deviations after 1 year are induced by the combined effect of (1) the occasional inclusion of poor quality $D_o(x)$, (2) lack of erosional differences $D_c - D_o$ to compensate for erroneous accretions at deeper water, and (3) the accumulation of small errors over time, induced by inaccurate $D_o(x)$. Mechanisms 1 and 2 dominate erroneous profile evolution in areas that are hardly exposed to wave dissipation, while the importance of mechanism 3 increases with decreasing water depth. Once again, this stresses the importance of setting an appropriate model response time, because the effect of both mechanisms 1 and 3 increases with decreasing model response time.

[36] In addition to w_E and w_A, their ratio, the depth power q and, to a smaller extent, T_u, the model response time also appears to be affected by the number of images that meet the acceptance criteria on $D_o(x)$ quality. The latter number varies for the two examined profile lines. Along the outer array $y = -1500$ m, the number of processed images over the period 15 September 1999 to 1 October 2000 exceeds the number for the central array $y = -130$ m with about 40%, yielding an increase in the cumulative bathymetry update time, defined as the sum of all time gaps $t_1 - t_0$ between successive good-quality images after potentially being reduced to a maximum T_u. The cumulative bathymetry update time amounts to 271 and 242 days for $y = -1500$ and $y = -130$ m, respectively, indicating an inherent decrease in the model response time for the outer array. This effect may have contributed to the accretion of sand in the shallow surf zone found for $y = -1500$ m.

[37] Despite the many processes included in the model, the heuristic scaling function F_s in equations (6) and (7) is essential to spatially adjust morphological growth rates and to provide sensible results, particularly near the shoreline. First, the applied wave transformation model was never meant to predict dissipation measures in the very shallow water depth near the shoreline, where the modeled root-mean square wave height is known to exceed the maximum wave height (equation (A5)) owing to an underestimation of dissipation [*Battjes and Janssen*, 1978] [see also *Aarninkhof et al.*, 2003]. Second, F_s ensures that the difference $D_c - D_o$ does not become unrealistically large in very shallow water, as here D_c theoretically becomes infinite, while the associated video-derived D_o will not. Finally, F_s minimizes model errors that tend to accumulate near the shoreline but are induced by errors at a more seaward location. For instance, in the synthetic example discussed in section 2.4, $w_A < 1 \times 10^{-5}$ ms^2/kg hampers the generation of bars, yielding insufficient wave dissipation D_c across the bars and hence an overestimation of D_c near the shoreline. Without the scaling function, this would cause an unrealistic deepening of the beach profile near the shoreline. Also, the removal of the h/h_0 dependent reduction of sediment fluxes by setting q to zero was found to result in unrealistic ''cliff'' formation near the shoreline [*Aarninkhof*, 2003]. On the whole, it appears that the adopted scaling function has the necessary ingredients to restrain bathymetric evolution in shallow water to realistic values. The scaling function implies that shoreline erosion or accretion may not be adequately simulated, hence limiting the model's applicability to environments where the shoreline tends to be more stable, such as dissipative beaches.

4.2. Calibration Issues

[38] The comparison with the Egmond field observations is highly dependent on the values of the model's free parameters (p, w_E, w_A, q, and T_u). The applied values were obtained by a manual search in that part of parameter space that we felt feasible for the problem at hand. Therefore we can neither claim these values to be the optimum values nor estimate their accuracy, for instance, through 95% confidence bands. Also, we cannot state that the Egmond values are the most likely values on another beach; they may serve as good starting values at best. Obtaining optimum values by means of an automated optimization algorithm while at the same time also obtaining a reliable estimate of the uncertainty in these optimum values is one of the research topics we are currently pursuing. At present, it is best to interpret p, w_E, w_A, q, and T_u as free model parameters that when

chosen appropriately, yield reasonable predictions of nearshore bathymetric evolution.

[39] The performance of SBM also depends on the criteria adopted to judge the quality of a cross-shore intensity profile (see also section 4.1). The Egmond values (Table 1) are empirical values that likely need to be changed when SBM is applied to another site or when another camera system is used. The criterion based on the width of the widest peak is, as an example, related to the width of the bars. At Duck, for instance, bars are considerably less wide than at Egmond [*Ruessink et al.*, 2003], and, as a consequence, we expect that $\sigma_{G,\max}$ has to be set to a somewhat lower value to indicate unrealistically wide dissipation peaks. In other words, what might be judged as "realistic" at Egmond might be "unrealistic" at Duck. Also, initial pre-processing BIM tests using data obtained with black-and-white cameras at Noordwijk, Netherlands [*Van Enckevort and Ruessink*, 2003], suggests that $I_{0,\min}$ needs to be lowered because the average intensity of such black-and-white images is lower than that of the color images used at Egmond. Although SBM contains a considerable number of empirical parameters, both in the preprocessing and bathymetry estimation module, the principle of bathymetry estimation from time-averaged videoed cross-shore intensity profiles is general.

4.3. Comparison to Phase-Speed Method

[40] The profile average root-mean square difference of 0.4 m between surveyed and SBM derived depth after 1 year of video-based depth updating compares favorably with a value of 0.9 m reported by *Stockdon and Holman* [2000] using video-based estimates of local phase speed using pixel intensity time series collected at Duck, North Carolina. One should not, however, put too much emphasis on the apparent better performance of our method. Both numbers may not be directly comparable, as *Stockdon and Holman* [2000] did not apply their phase-speed technique at Egmond, nor did we apply our technique to Duck data. In addition, the emphasis in our technique is on morphological evolution as opposed to the narrowly defined depth inversion in the phase-speed method. The principle of bathymetry estimation at Duck by means of wave dissipation patterns has been demonstrated before by *Aarninkhof et al.* [1997], albeit with a predecessor of SBM. It is, however, obvious that the phase-speed method and our dissipation method are complementary. While the phase-speed method works well in the offshore and trough areas and breaks down in the breaker zone, the dissipation method is most accurate across bars under breaking waves and is more troubled in the offshore and trough areas, where the dissipation signal is low. The combination of the two techniques may yield accurate bathymetry estimates across the entire depth profile and is a key topic for future research.

5. Conclusions

[41] A new technique (SBM) has been developed to estimate the temporal evolution of cross-shore depth profiles from time-averaged (over many wave periods) videoed cross-shore intensity profiles. The technique is based on the close correspondence between observed Gaussian-shaped intensity profiles, caused by the preferential wave breaking on sandbars, and similar profiles of the dissipation of the wave roller, as predicted by a standard wave transformation model. Differences between these observed and predicted dissipation proxies force a sediment exchange between the seabed and a buffer layer above the bed. A positive difference between modeled and observed dissipation drives an upward directed erosional sediment flux from the seabed to the buffer layer, causing local erosion of the seabed and a local increase in the sediment concentration in the buffer layer. A negative difference results in the opposite effect, driving a downward directed accretional sediment flux, which yields accretion of the seabed and a decrease in the sediment concentration in the buffer layer. Cross-shore gradients in this concentration drive the horizontal redistribution of sediment within the buffer layer from regions of high concentration (sediment surplus in the buffer layer due to seabed erosion) to regions of low concentration (sediment shortage in the buffer layer due to seabed accretion). The technique operates on a time series of (hourly) intensity profiles and aims for a partial update of the depth profile between consecutive intensity profiles. In this way, the technique resolves the pattern in depth change on a morphological timescale (including overall gain or loss of sediment) and does not focus on the (noisy) characteristics of a single intensity profile.

[42] The technique was tested using 1 year of hourly video data collected at Egmond aan Zee, Netherlands. The dominant morphological changes observed from ground truth data, including the shoreward migration of the outer bar and the net sediment gain in the profile, were reproduced reasonably well, except in the intertidal zone. Root-mean square differences between surveyed and SBM derived depth after 1 year of video-based depth updating with an average of about 70 intensity profiles per month were smallest ($\sim$0.2 m) on the inner bar and largest ($\sim$0.6 m) in the outer bar trough, with a profile average value of about 0.4 m.

[43] The distinct advantages of our technique are that it is relatively cheap compared to alternative direct measurement techniques, it provides good spatial resolution and coverage, and, perhaps most importantly, it works well during storm conditions when morphological changes are most prominent. Drawbacks include the need to have additional knowledge of offshore wave parameters (height, period, direction) and water level to drive the wave transformation model, and the assumption that the bathymetry does not change in the absence of waves. In addition, our method does not work that well in those parts of the cross-shore profile where the dissipation signal is low or infrequent, such as offshore of the surfzone and in the deep trough areas. This points to the complimentary nature of our methodology and the phase-speed method [*Stockdon and Holman*, 2000], as this method appears to work well where our method does not, and vice versa. While perhaps not of comparable accuracy to conventional survey techniques, for which typical errors less than about 0.3 m are reported [e.g., *Birkemeier and Mason*, 1984; *Ruessink et al.*, 2004], SBM provides reasonably accurate depth estimates over extended periods of time (>months–years) with a high temporal resolution (say, hours to days). This will make available time series of nearshore depth evolution unob-

tainable otherwise that, no doubt, will aid in the formulation and testing of nearshore system models.

Appendix A: Wave Transformation Model

[44] The wave model consists of two coupled differential equations that describe the time-averaged (over many wave periods) cross-shore evolution of organized wave energy E and roller energy E_r. With the assumption that the wave field is narrow-banded in frequency and direction, these balances are

$$\frac{\mathrm{d}}{\mathrm{d}x}\left(\frac{1}{8}\rho g H_{\mathrm{rms}}^2 c_g \cos\bar{\theta}\right) = -D_b \tag{A1}$$

and [*Nairn et al.*, 1990; *Stive and De Vriend*, 1994]

$$\frac{\mathrm{d}}{\mathrm{d}x}\left(2E_r c\cos\bar{\theta}\right) = -D_r + D_b, \tag{A2}$$

respectively, with breaking-wave dissipation D_b [*Baldock et al.*, 1998] and roller-dissipation D_r given by

$$D_b = 0.25\rho g f_p \exp^{-(H_b/H_{\mathrm{rms}})^2}\left(H_b^2 + H_{\mathrm{rms}}^2\right) \tag{A3}$$

$$D_r = 2\beta g E_r / c, \tag{A4}$$

respectively, where [*Battjes and Stive*, 1985]

$$H_b = \frac{0.88}{k}\tanh\left(\frac{\gamma k h}{0.88}\right). \tag{A5}$$

Here ρ is water density, g is gravitational acceleration, and H_{rms} is the root-mean square wave height. The group velocity c_g, the phase speed c, and the wave number k are evaluated with linear theory at the peak frequency f_p using the local water depth h. The cross-shore evolution of the mean wave angle $\bar{\theta}$ (relative to shore normal) follows from offshore measurements using Snell's law. As in the work of *Aarninkhof and Ruessink* [2004], default values for the model's free parameters were used: the wave height to depth ratio $\gamma = 0.5 + 0.4\tanh(33 s_0)$ [*Battjes and Stive*, 1985], where s_0 is the offshore wave steepness, and the roller parameter $\beta = 0.1$ [*Reniers and Battjes*, 1997]. Integration of equations (A1) and (A2) from an offshore position, where H_{rms}, peak period $T_p = 1/f_p$, $\bar{\theta}$, and water level ζ are available, shoreward using one-sided finite differences yields the cross-shore distribution of D_r, the model-predicted dissipation proxy used for $D_c(x)$.

[45] **Acknowledgments.** S. G. J. A. was funded by the Interfaculty Research Centre "Observation of the Earth and Earth's crust" at Delft University of Technology, the Dutch Ministry of Transport and Public Works (Rijkswaterstaat), the Delft Cluster Project Coasts (03.01.03), and the EU-funded CoastView project under contract EVK3-CT-2001-0054. B. G. R. was supported by the Netherlands Organisation for Scientific Research under project 864.04.007. The Argus video technique has been developed with funds generated by the Coastal Imaging Laboratory, Oregon State University. The authors wish to acknowledge the two anonymous reviewers for their thought-provoking comments, and Rob Holman for actively and generously stimulating the collaboration within the worldwide Argus research group.

References

Aarninkhof, S. G. J. (2003), Nearshore bathymetry derived from video imagery, Ph.D. thesis, Civ. Eng., Delft Univ. of Technol., Delft, Netherlands.

Aarninkhof, S. G. J., and B. G. Ruessink (2001), Video observations of wave breaking and the implication for wave decay modelling, paper presented at Coastal Dynamics'01, Am. Soc. of Civ. Eng., Reston, Va.

Aarninkhof, S. G. J., and B. G. Ruessink (2004), Video observations and model predictions of depth-induced wave dissipation, *IEEE Trans. Geosci. Remote Sens.*, *42*, 2612–2622.

Aarninkhof, S. G. J., P. C. Janssen, and N. G. Plant (1997), Quantitative estimations of bar dynamics from video images, paper presented at Coastal Dynamics'97, Am. Soc. of Civ. Eng., Reston, Va.

Aarninkhof, S. G. J., I. L. Turner, T. D. T. Dronkers, M. Caljouw, and L. Nipius (2003), A video-based technique for mapping intertidal beach bathymetry, *Coastal Eng.*, *49*, 275–289.

Alpers, W., and I. Hennings (1984), A theory of the imaging mechanism of underwater bottom topography by real and synthetic aperture radar, *J. Geophys. Res.*, *89*, 10,529–10,546.

Baldock, T. E., P. Holmes, S. Bunker, and P. Van Weert (1998), Cross-shore hydrodynamics within an unsaturated surf zone, *Coastal Eng.*, *34*, 173–196.

Battjes, J. A., and J. P. F. M. Janssen (1978), Energy loss and set-up due to breaking of random waves, paper presented at 16th International Conference on Coastal Engineering, Am. Soc. of Civ. Eng., Reston, Va.

Battjes, J. A., and M. J. F. Stive (1985), Calibration and verification of a dissipation model for random breaking waves, *J. Geophys. Res.*, *90*, 9159–9167.

Bell, P. S. (1999), Shallow water bathymetry derived from an analysis of X-band marine radar images of waves, *Coastal Eng.*, *37*, 513–527.

Benny, A. H., and G. J. Dawson (1983), Satellite imagery as an aid to bathymetric charting in the Red Sea, *Cartogr. J.*, *20*, 5–16.

Bierwirth, P. N., T. J. Lee, and R. V. Burne (1993), Shallow sea-floor reflectance and water depth derived by unmixing multispectral imagery, *Photogramm. Eng. Remote Sens.*, *59*(3), 331–338.

Birkemeier, W. A., and C. Mason (1984), The CRAB: A unique nearshore surveying vehicle, *J. Surv. Eng.*, *110*, 1–7.

Calkoen, C. J., G. J. Wensink, and G. H. F. M. Hesselmans (1993), ERS-1 SAR imagery to optimize the NOURTEC shipbased bathymetric survey: Feasibility study, *H 1875*, 23 pp., Delft Hydraul., Delft, Netherlands.

Dugan, J. P., C. C. Piotrowski, and J. Z. Williams (2001), Water depth and surface current retrievals from airborne optical measurements of surface gravity wave dispersion, *J. Geophys. Res.*, *106*, 16,903–16,915.

Green, E. P., A. J. Edwards, and P. J. Mumby (2000), Mapping bathymetry, in *Remote Sensing: Handbook for Tropical Coastal Management*, edited by A. J. Edwards, pp. 219–233, UNESCO Publ., Paris.

Grilli, S. T. (1998), Depth inversion in shallow water based on nonlinear properties of shoaling periodic waves, *Coastal Eng.*, *35*, 185–209.

Haller, M. C., and D. R. Lyzenga (2003), Comparison of radar and video observations of shallow water breaking waves, *IEEE Trans. Geosci. Remote Sens.*, *41*, 832–844.

Hennings, I. (1990), Radar imaging of submarine sand waves in tidal channels, *J. Geophys. Res.*, *95*, 9713–9721.

Holman, R. A., A. H. J. Sallenger, T. C. Lippmann, and J. W. Haines (1993), The application of video image processing to the study of nearshore processes, *Oceanography*, *6*(3), 78–85.

Irish, J. L., and W. J. Lillycrop (1999), Scanning laser mapping of the coastal zone: The SHOALS system, *ISPRS J. Photogramm. Remote Sens.*, *54*, 123–129.

Kennedy, A. B., R. A. Dalrymple, J. T. Kirby, and Q. Chen (2000), Determination of inverse depths using direct Boussinesq modeling, *J. Waterw. Port Coastal Ocean Eng.*, *126*, 206–214.

Kingston, K. S., B. G. Ruessink, I. M. J. Van Enckevort, and M. A. Davidson (2000), Artificial neural network correction of remotely sensed sandbar location, *Mar. Geol.*, *169*, 137–160.

Lippmann, T. C., and R. A. Holman (1989), Quantification of sand bar morphology: A video technique based on wave dissipation, *J. Geophys. Res.*, *94*, 995–1011.

Lyzenga, D. R. (1985), Shallow-water bathymetry using combined lidar and passive multispectral scanner data, *Int. J. Remote Sens.*, *6*, 115–125.

McGregor, J. A., E. Murray Poulter, and M. J. Smith (1998), S band Doppler radar measurement of bathymetry, wave energy fluxes, and dissipation across an offshore bar, *J. Geophys. Res.*, *103*(C9), 18,779–18,789.

Misra, S., A. B. Kennedy, and J. T. Kirby (2003), An approach to determining nearshore bathymetry using remotely sensed ocean surface dynamics, *Coastal Eng.*, *47*, 265–293.

Nairn, R. B., J. A. Roelvink, and H. N. Southgate (1990), Transition zone width and implications for modelling surfzone hydrodynamics, paper

presented at 22nd International Conference on Coastal Engineering, Am. Soc. of Civ. Eng., Reston, Va.

Reniers, A. J. H. M., and J. A. Battjes (1997), A laboratory study of longshore currents over barred and non-barred beaches, *Coastal Eng.*, *30*, 1–22.

Ruessink, B. G., I. M. J. Van Enckevort, K. S. Kingston, and M. A. Davidson (2000), Analysis of observed two- and three-dimensional nearshore bar behaviour, *Mar. Geol.*, *169*, 161–183.

Ruessink, B. G., P. S. Bell, I. M. J. Van Enckevort, and S. G. J. Aarninkhof (2002), Nearshore bar crest location quantified from time-averaged X-band radar images, *Coastal Eng.*, *45*, 19–32.

Ruessink, B. G., K. M. Wijnberg, R. A. Holman, Y. Kuriyama, and I. M. J. Van Enckevort (2003), Intersite comparison of interannual nearshore bar behavior, *J. Geophys. Res.*, *108*(C8), 3249, doi:10.1029/2002JC001505.

Ruessink, B. G., I. M. J. Van Enckevort, and Y. Kuriyama (2004), Nonlinear principal component analysis of nearshore bathymetry, *Mar. Geol.*, *108*, 185–197.

Sandidge, J. C., and R. J. Holyer (1998), Coastal bathymetry from hyperspectral observations of water radiance, *Remote Sens. Environ.*, *65*, 341–352.

Stive, M. J. F., and H. J. De Vriend (1994), Shear stress and mean flow in shoaling and breaking waves, paper presented at 24th International Conference on Coastal Engineering, Am. Soc. of Civ. Eng., Reston, Va.

Stockdon, H. F., and R. A. Holman (2000), Estimation of wave phase speed and nearshore bathymetry from video imagery, *J. Geophys. Res.*, *105*, 22,015–22,033.

Van Enckevort, I. M. J., and B. G. Ruessink (2001), Effects of hydrodynamics and bathymetry on video estimates of nearshore sandbar position, *J. Geophys. Res.*, *106*, 16,969–16,979.

Van Enckevort, I. M. J., and B. G. Ruessink (2003), Video observations of nearshore bar behaviour: Part 1. Alongshore uniform variability, *Cont. Shelf Res.*, *23*, 501–512.

Vogelzang, J., G. J. Wensink, C. J. Calkoen, and M. W. A. Van der Kooij (1997), Mapping submarine sand waves with multiband imaging radar: 2. Experimental results and model comparison, *J. Geophys. Res.*, *102*, 1183–1192.

Williams, W. W. (1947), The determination of gradients on enemy-held beaches, *Geogr. J.*, *109*, 76–90.

S. G. J. Aarninkhof and J. A. Roelvink, Marine and Coastal Management, WL|Delft Hydraulics, P. O. Box 177, N-2600 MH Delft, Netherlands. (stefan.aarninkhof@wldelft.nl; dano.roelvink@wldelft.nl)

B. G. Ruessink, Department of Physical Geography, Faculty of Geosciences, Institute for Marine and Atmospheric Research, Utrecht University, P. O. Box 80.115, N-3508 TC Utrecht, Netherlands. (g.ruessink@geo.uu.nl)